

Yu-Shiba-Rusinov states in the s -wave superconducting kagome Hubbard model: Self-consistent Bogoliubov-de Gennes calculations

Shuaibo Ding,¹ Yunfei Bai,¹ Wenhui Zhang,² A. A. Shanenko,³ and Yajiang Chen^{1,*}

¹*Department of Physics, Zhejiang Sci-Tech University, 310018 Hangzhou, China*

²*School of Electronic Engineering, Nanjing Xiaozhuang University, Nanjing, China*

³*HSE University, 101000 Moscow, Russia*

(Dated: March 12, 2024)

The Yu-Shiba-Rusinov (YSR) states in kagome superconductors have been studied recently in theory and experiments. However, more details of local superconductivity around the YSR states in kagome superconductors and the existence of the related first-order phase transition remain unclear. Based on the self-consistent Bogoliubov-de Gennes equations for the s -wave superconducting kagome Hubbard model, we show that first-order phase transitions occur when varying the spin-magnetic interaction J of the magnetic impurity, and discontinuities of hysteresis loops in the plots of the local pair potential versus J happen at the upper and lower critical interactions J_{c1} and J_{c2} , rather than the conventional critical interaction J_c . The minimal energy of the stable YSR state $E_{\text{YSR,min}}$ is non-zero for the chemical potential at the van Hove singularities, Dirac point, and the flat band. Furthermore, J_{c1} , J_{c2} , and $E_{\text{YSR,min}}$ are dependent on the chemical potential and the superconducting coupling interaction.

I. INTRODUCTION

Kagome metals and superconductors have been investigated intensively because of rich exotic properties induced by their geometric frustration and strongly correlated interactions. For instance, the theoretically predicted [1–4] flat band (FB), van Hove singularity (VHS), Dirac point (DP), and multiband feature of the energy spectrum in kagome Hubbard model have been experimentally verified in the high-quality kagome metals, e.g., Fe_3Sn_2 [5], AV_3Sb_5 (A=K, Rb, Cs) [6–8], YCr_6Ge_6 [9], and AV_6Sn_6 (A=Y, Gd) [10]. And, angle-resolved photoemission spectroscopy [7] and measurements of resistivity and magnetic susceptibility [11] have revealed multiple electron orders resulting from complex electron interactions in these materials, such as topological order and charge-density-wave order. Moreover, unconventional superconductivity has been predicted [2] and observed in CsV_3Sb_5 [12], including nematic phase [13], pair-density-wave order [14], M-like pressure-dependence T_c behavior [15], and the superconducting order parameter with possible two-band ($s+s$)-wave symmetry [16, 17], etc.

Recently, the Yu-Shiba-Rusinov (YSR) states [18–21], as a promising candidate for constructing Majorana zero modes and qubits [22–26], have been studied by doping magnetic impurities in kagome superconductors both theoretically [27] and experimentally [16]. The YSR states are known to be the bound in-gap states near magnetic impurities. The Bogoliubov-de Gennes (BdG) calculations [27] for the s -wave superconducting kagome Hubbard model have shown that when the coupling between a magnetic impurity and superconductor J is weak enough, Cooper pairs are not destroyed around the impurity. However, when J crosses its critical value J_c (corre-

sponding to the zero-energy YSR state), one observes the local reconstruction of the ground state due to the pair breaking in the vicinity of the magnetic impurity (see the related explanations in Ref. 28). The most interesting feature of these results [27] is that J_c is very sensitive to FB, VHS, and DP singularities of the single-particle spectrum of the kagome model.

However, the BdG study of Ref. 27 assumes a uniform distribution of the superconducting condensate. In other words, this approach is not self-consistent and cannot capture the common depression and the related $0-\pi$ transition of the s -wave superconducting order parameter near magnetic impurities [21, 28, 29]. Such local depression of the superconducting condensate has been detected around the magnetic Cr cluster in CsV_3Sb_5 by scanning tunneling microscopy [16]. Self-consistent BdG calculations usually demonstrate that a change in the coupling between the magnetic impurity and s -wave superconductor results in a first-order phase transition [29], in which a discontinuous jump occurs in the local superconducting order parameter around the impurity. However, this particular type of the first-order phase transition has not been revealed or investigated in the s -wave superconducting kagome Hubbard model [27]. Our current study addresses this gap.

In the present work, by numerically solving the self-consistent BdG equations, we systematically investigate the properties of the YSR state in an s -wave superconducting kagome Hubbard model. [Notice that the related system can be realized due to the proximity effect by constructing an artificial kagome lattice on top of an s -wave superconductor [30, 31].] Our numerical results demonstrate the first-order phase transition related to the formation of the YSR states with the two critical spin-magnetic interactions J_{c1} and J_{c2} corresponding to the metastable zero-energy YSR states. Parameters of the transition are significantly affected by the superconducting coupling strength g and the chemical potential

* yjchen@zstu.edu.cn

μ (i.e., by singularities in the energy-spectrum structure of the kagome lattice). The minimal stable energy of the YSR state is non-zero when the chemical potential approaches the single-particle energies of the VHS, DP, and FB.

The paper is organized as follows. In Sec. II, we outline the formalism of the self-consistent BdG equations for the s -wave superconducting kagome Hubbard model with a magnetic impurity. In Sec. III we first discuss numerical results obtained for the related kagome lattice at zero spin-magnetic coupling $J = 0$. Then, using this data as a reference, we proceed to the calculations of the local pair potential in the vicinity of the impurity, the corresponding YSR energy, and the system free energy as functions of J for different values of g and μ . Our conclusions are given in Sec. IV.

II. THEORETICAL FORMALISM

The starting point of our investigation is the s -wave superconducting kagome Hubbard model with a single magnetic impurity. Its grand-canonical Hamiltonian is given by [32]

$$H = \sum_{ij\sigma} H_{ij\sigma} c_{i\sigma}^\dagger c_{j\sigma} - \frac{g}{2} \sum_{i\sigma\sigma'} c_{i\sigma}^\dagger c_{i\sigma'}^\dagger c_{i\sigma'} c_{i\sigma}, \quad (1)$$

where the indices $i = \{i_x, i_y\}$ and $j = \{j_x, j_y\}$ enumerate the sites of the two-dimensional kagome lattice; $c_{i\sigma}$ and $c_{i\sigma}^\dagger$ are the fermionic annihilation and creation operators for electrons at the site i with the spin projection $\sigma = \pm$ in units of $\hbar/2$; $g (> 0)$ is the s -wave pair coupling; and $H_{ij\sigma}$ is the matrix element of the single-particle Hamiltonian. The latter, for the case of the nearest-neighbor approximation, reads $H_{ij\sigma} = -t\delta_{\langle ij \rangle} - [\mu - (K - \sigma J)\delta_{i0}] \delta_{ij}$ [33], with t the nearest-neighbor hopping parameter and K the scattering potential coupling (nonmagnetic). The magnetic impurity is located at $i_0 = \{i_{0x}, i_{0y}\}$.

Within the mean-field approximation [34], the Hamiltonian given by Eq. (1) acquires the form

$$H_{\text{eff}} = \sum_{ij\sigma} H_{ij\sigma} c_{i\sigma}^\dagger c_{j\sigma} + \sum_{i\sigma} U_{i\sigma} c_{i\sigma}^\dagger c_{i\sigma} + \sum_i \left(\Delta_i c_{i\uparrow}^\dagger c_{i\downarrow}^\dagger + \Delta_i^* c_{i\downarrow} c_{i\uparrow} \right) \quad (2)$$

with $U_{i\sigma}$ and Δ_i being the Hartree-Fock potential and pair potential, respectively. Using the Bogoliubov unitary transformation [27] $c_{i\sigma} = \sum_n (u_{in\sigma} \gamma_{n\sigma} - \sigma v_{in\sigma}^* \gamma_{n\bar{\sigma}}^\dagger)$ with $\bar{\sigma} = -\sigma$, the effective Hamiltonian Eq. (2) can be diagonalized as $H = \sum_{n\sigma} \varepsilon_{n\sigma} \gamma_{n\sigma}^\dagger \gamma_{n\sigma} + E_0$, where $\varepsilon_{n\sigma}$ is the quasiparticle energy, $u_{in\sigma}$ and $v_{in\sigma}$ are the spatial particle- and hole-like quasiparticle wavefunctions, $\gamma_{n\sigma}$ and $\gamma_{n\bar{\sigma}}^\dagger$ are the quasiparticle creation and annihilation operators satisfying the fermionic canonical commutation relations, and $E_0 = \sum_i |\Delta_i|^2/g - \sum_{in\sigma} |v_{in\bar{\sigma}}|^2 \varepsilon_{n\sigma}$ is the

ground state energy [35]. The wave functions $u_{in\sigma}$ and $v_{in\sigma}$ obey the Bogoliubov-de Gennes (BdG) equations

$$\sum_j (H_{ij\sigma} + U_{j\sigma} \delta_{ij}) u_{in\sigma} + \Delta_i v_{in\bar{\sigma}} = \varepsilon_{n\sigma} u_{in\sigma} \quad (3a)$$

$$\Delta_i^* u_{in\sigma} - \sum_j (H_{ij\bar{\sigma}}^* + U_{j\bar{\sigma}}^* \delta_{ij}) v_{jn\bar{\sigma}} = \varepsilon_{n\sigma} v_{in\bar{\sigma}}. \quad (3b)$$

The solutions of the BdG equations Moreover, the free energy \mathcal{F} and the spatial electron density n_{ei} read [36]

$$\mathcal{F} = \sum_{n\sigma} f_{n\sigma} \varepsilon_{n\sigma} + \sum_i |\Delta_i|^2/g - \sum_{in\sigma} |v_{in\bar{\sigma}}|^2 \varepsilon_{n\sigma} \quad (4a)$$

$$n_{ei} = \sum_{n\sigma} \left[|u_{in\sigma}|^2 f_{n\sigma} + |v_{in\sigma}|^2 (1 - f_{n\bar{\sigma}}) \right]. \quad (4b)$$

The BdG equations are solved together with the self-consistency equations for $U_{i\sigma}$ and Δ_i given by

$$U_{i\sigma} = -g \sum_n \left[|u_{in\sigma}|^2 f_{n\sigma} + |v_{in\sigma}|^2 (1 - f_{n\bar{\sigma}}) \right] \quad (5a)$$

$$\Delta_i = g \sum_n \left[u_{in\uparrow} v_{in\downarrow}^* (1 - f_{n\uparrow}) - u_{in\downarrow} v_{in\uparrow}^* f_{n\downarrow} \right] \quad (5b)$$

with the Fermi-Dirac quasiparticle distribution $f_{n\sigma} = f(\varepsilon_{n\sigma})$. The summation in Eq. (5a) runs over all positive-energy quasiparticles, while for Δ_i the summation includes only the quasiparticle states with positive energies inside the Debye energy ($\hbar\omega_D$) window, i.e., $0 \leq \varepsilon_{n\sigma} \leq \hbar\omega_D$ [34]. For simplicity, below the Hartree-Fock potential is ignored as its effect is reduced only to a shift in the chemical potential that does not change the general features of our results. [37–41]

One may note that the 4-by-4 set of the BdG equations given by Eq. (3) is separated into the two sets of the 2-by-2 BdG equations for $\varepsilon_{n,\uparrow}$ and $\varepsilon_{n,\downarrow}$, respectively. The BdG solutions corresponding to $\varepsilon_{n\uparrow}$ and $\varepsilon_{n\downarrow}$ are connected by the relations $\varepsilon_{n\downarrow} = -\varepsilon_{n\uparrow}$, $u_{in\downarrow} = v_{in\downarrow}^*$, and $v_{in\uparrow} = -u_{in\uparrow}^*$. Thus, to simplify the numerical procedure, one can solve the 2-by-2 BdG equations, say, for $\varepsilon_{n\uparrow}$ and, then, the above relations can be utilized to get such solutions for $\varepsilon_{n\downarrow}$.

To consider the properties of the YSR states in the vicinity of the selected single-particle energies corresponding to the VHS, DP and FB, we follow the choice of Ref. [27] and consider the chemical potential μ as an external parameter, rather than the average electron filling level ($\bar{n}_e = \sum_i n_{ei}/N_{\text{tot}}$, with N_{tot} being the total number of sites) as in Refs. [42, 43]. Then, the procedure of obtaining a self-consistent solution is as follows: first, an initial guess for the pair potential Δ_i is chosen; second, the 2-by-2 BdG equations are solved for a given value of μ ; third, the obtained solutions of the corresponding eigenvalue problem are used to get a new spatial distribution of the pair potential. This procedure is repeated until the numerical convergence. After the convergence, utilizing the self-consistent solutions of the BdG equations, we calculate the remaining pertinent

physical quantities, including the free energy \mathcal{F} and electron density n_{ei} given by Eqs. (4) and (5b).

In our work, the energy-related quantities (e.g., g , μ , K , J , Δ_i and \mathcal{F}) are measured in units of the nearest-neighbor hopping parameter t . We consider a kagome lattice with $N \times N = 20 \times 20$ primitive unit cells under the periodic boundary conditions at zero temperature $T = 0$. The chosen value of N is sufficiently large to reach the regime of an isolated YSR state. The doped magnetic impurity is set at the site $i_0 = \{19, 20\}$ marked by the red star in Fig. 1(a). For our calculations, we adopt $K = 0$ and $\hbar\omega_D = 8$. Since the single-particle energy interval of the non-superconducting kagome model is from $-4t$ to $2t$, $\hbar\omega_D$ is large enough to include all the positive quasiparticle states when calculating the pair potential given by Eq. (5b). However, this choice of the parameters of the model is not critical for our general conclusions.

III. RESULTS AND DISCUSSIONS

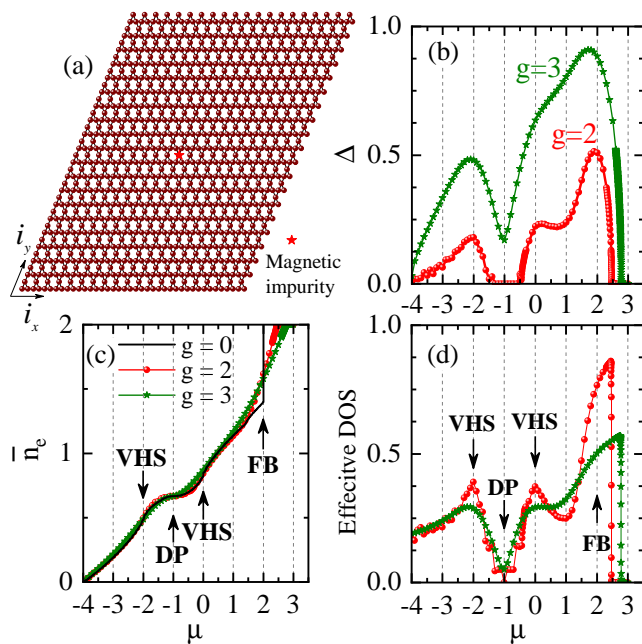


FIG. 1. (Color online) (a) Sketch of the kagome lattice used in our calculations and containing 20×20 primitive unit cells with a single magnetic impurity marked by the red star; (b-d) The self-consistent impurity-free numerical results for the pair potential Δ , filling level \bar{n}_e and the effective density of states ($d\bar{n}_e/d\mu$ in unit of $1/t$) as functions of the chemical potential μ for $g = 2$ (red spheres) and 3 (green stars) at $T = 0$. In panel (c) one can also see \bar{n}_e for $g = 0$. The particular values of μ corresponding to the van Hove singularities (VHS), Dirac point (DP), and flat band (FB) are marked in panels (c, d) by arrows.

To have an idea about the energy spectrum and pertinent quantities of the impurity-free attractive kagome

Hubbard model, Figs. 1(b-d) demonstrate the self-consistent numerical results for the pair potential Δ , the filling level \bar{n}_e , and the effective density of states (DOS, defined as $d\bar{n}_e/d\mu$ in unit of $1/t$) as functions of the chemical potential μ for the case $J = 0$. The curves with red spheres and green stars correspond to the couplings $g = 2$ and 3, respectively. In addition, the black solid curve in Fig. 1(c) shows \bar{n}_e calculated for the normal state with $g = 0$. The selected values of the chemical potential corresponding to the VHS, DP, and FB regimes are marked by arrows in panels (c,d), i.e., $\mu = -2$ (VHS), -1 (DP), 0 (VHS), and 2 (FB).

We notice that the impurity-free system exhibits a homogeneous pair potential, which changes significantly with μ , as seen from Fig. 1(b). The filling level \bar{n}_e is also strongly dependent on μ and specified by a monotonous increase with μ , i.e. electrons fill the lattice with rising μ , see Fig. 1(c). However, the dependence of the pair potential on μ is not trivial due to the presence of the special single-particle energies related to the VHS, DP, and FB. In particular, for $g = 2$, the pair potential Δ exhibits three local maxima at the VHS and FB points, which are associated with the corresponding increases in the effective DOS. The two VHS maxima related are not the same because the VHS points correspond to different electron-filling levels. The superconductive correlations vanish around the DP in the interval $-1.3 < \mu < -0.6$ (for $g = 2$) due to a significant drop of the effective DOS to zero at the DP, see Fig. 1(d). It is also worth mentioning that Δ is nonzero up to $\mu_{\max} = 2.47$ which exceeds the chemical potential $\mu = 2$ at the FB by about 24%. This feature appears due to the smearing of the FB in the presence of the superconductive correlations. This smearing is also visible in the data for the electron filling level in Fig. 1(c). The derivative of \bar{n}_e with respect to μ , i.e., the effective DOS in Fig. 1(d), is no longer infinite at $\mu = 2$ for $g > 0$, and it drops to zero only at $\mu_{\max} = 2.47$.

For $g = 3$ (represented by the curves with green stars in Fig. 1), the pair potential is significantly enhanced as compared to the case of $g = 2$. In more detail, the two local maxima related to the VHS (at $\mu = 0$) and the FB merge in one pronounced peak of Δ . In addition, a drop of Δ to zero near the DP, observed for $g = 2$, becomes a finite local minimum at $\mu = -1$ for $g = 3$. The full occupation by electrons occurs at $\mu_{\max} = 2.75$ which is larger than the corresponding maximum value of the chemical potential 2.47 at $g = 2$. One may notice that around the FB there are distinctive shifts between the peak positions of Δ and the effective DOS. We expect that this can occur due to the proximity of the VHS increase of Δ near $\mu = 0$.

Now we turn to the interplay of the classical magnetic impurity with the superconductive correlations. The related self-consistent results are shown in Fig. 2 for $g = 2$ and $T = 0$. In particular, the local pair potential Δ_{imp} at the impurity location is shown versus the spin-magnetic coupling J in Figs. 2(a-c) for $\mu = -2$ (VHS), 0 (VHS), and 2 (FB). The energies of the YSR state E_{YSR} are

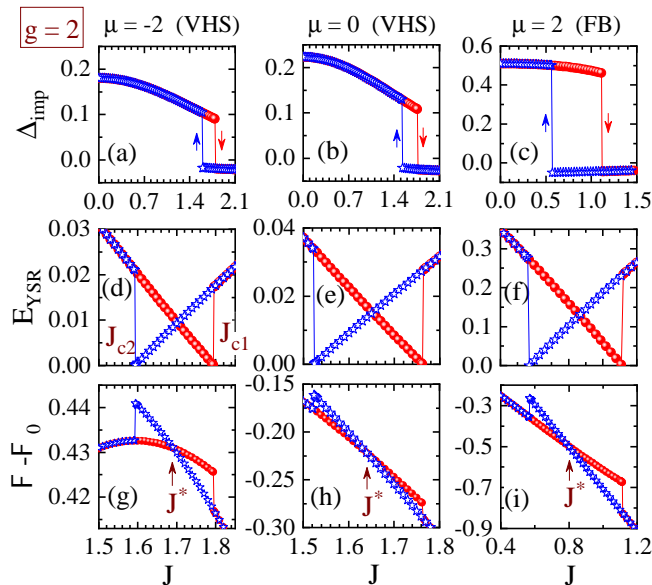


FIG. 2. (Color online) The pair potential at the impurity location Δ_{imp} (a-c), the YSR state energy E_{YSR} (d-f), and the free energy \mathcal{F} (g-i) versus the coupling J for $\mu = -2$ (VHS), 0 (VHS) and 2 (FB) at $g = 2$ and $T = 0$. The curves with red spheres and blue stars represent the ascending and descending branches, respectively, see the blue and red arrows shown in panels (a-c). J_{c1} and J_{c2} highlighted in panel (d) are the upper and lower critical interactions for $E_{\text{YSR}} = 0$. J^* marks the point of the first-order transition in panels (g-i) and corresponds to the minimal stable YSR energy.

given versus J for the VHS, DP, and FB regimes in panels (d-f). Finally, the free energy \mathcal{F} as a function of J is demonstrated in panels (g-i) for the same values of μ . The free energy \mathcal{F} is shown relative to \mathcal{F}_0 , the system free energy at $J = 0$. To clearly identify the presence of the first-order transition, the calculations are done in ascending and descending manners, using the pair potential Δ_i calculated at the preceding step as the initial guess for the new step corresponding to a new (larger or smaller) value of J . The curves with red spheres in Fig. 2 represent our results obtained in the ascending procedure while the blue stars are calculated in the descending procedure. Notice that the range of J -values is deliberately enlarged in panels (d-i).

As compared with Ref. [27], the most distinctive feature in Fig. 2 is the presence of the first-order transition: one can see the discontinuities and the related hysteresis loops of Δ_{imp} , E_{YSR} , and $\mathcal{F} - \mathcal{F}_0$. The jump in the ascending branch occurs at $J = J_{c1}$ while the corresponding jump in the descending branch takes place at $J_{c2} < J_{c1}$. From Figs. 2(a-c) one can learn that Δ_{imp} is positive for both the ascending and descending branches for $J < J_{c1}$ and J_{c2} . However, irrespective of the particular branch, Δ_i becomes negative above the corresponding jump point. This is similar to the $0-\pi$ transition in the phase of the pair potential reported previously for the case of a magnetic impurity in the triangular lattice [28].

One can also see that below the transition region, Δ_{imp} decreases with increasing J , as seen for $\mu = -2, 0$, and 2 in Figs. 2(a-c). This agrees with the earlier results of Refs. [21, 29].

From Fig. 2(d-f), we find that $E_{\text{YSR}} = 0$ $J = J_{c1}$ and J_{c2} , which differs significantly from the result $J_c = 1/\pi D(\mu)$ (with $D(\mu)$ the DOS per spin at μ) obtained in Refs. [21, 27] within non self-consistent calculations, based on the assumption of a uniform pair potential, for the nonmagnetic potential coupling $K = 0$. Our numerical study reveals that J_{c1} and J_{c2} are very sensitive to μ . For J_{c1} we get 1.79 ($\mu = -2$, VHS), 1.76 ($\mu = 0$, VHS), and 1.11 ($\mu = 2$, FB). For J_{c2} one obtains 1.59 ($\mu = -2$, VHS), 1.52 ($\mu = 0$, VHS), and 0.57 ($\mu = 2$, FB). Moreover, the difference $J_{c1} - J_{c2}$ also depends strongly on μ : $J_{c1} - J_{c2} = 0.20, 0.24$, and 0.54 for $\mu = -2, 0$, and 2, respectively. It is instructive to compare the critical value $J_c = 1/\pi D(\mu)$, given above and obtained in the papers [21, 27], with our numerical results for J_{c1} and J_{c2} . To estimate $D(\mu)$, one can employ the effective DOS of our kagome model in Fig. 1(d). This results in $J_c = 1.63, 1.71$, and 0.83 for $\mu = -2, 0$ and 2, respectively. For all of these estimates we obviously have $J_{c1} < J_c < J_{c2}$.

To determine the stable YSR states, one needs to compare the free energies of the ascending (red spheres) and descending (blue stars) branches. Then, according to the standard prescriptions of the thermodynamics, the stable YSR states correspond to the minimal free energy. One can see from Figs. 2(g-i) that the free energies of the ascending and descending branches cross each other at J^* , which is the point of the first-order transition occurring in the system with changing the spin-magnetic interaction J . At the same time, according to Figs. 2(a-c), this is the $0-\pi$ transition in the phase of the pair potential that also appears for a magnetic impurity in the triangular lattice [28]. For $\mu = -2, 0$ and 2, one finds from Figs. 2(g-i) $J^* = 1.69, 1.64$ and 0.80 . Notice that these values are very close to the estimates of $J_c = 1/\pi D(\mu)$ obtained by substituting the results of Fig. 1(d) for $D(\mu)$. However, and this is more important and different from the non self-consistent results, the stable YSR states have nonzero energies $E_{\text{YSR}} \neq 0$.

Furthermore, the same results for $g = 3$ are shown in Fig. 3 with $\mu = -2$ (VHS), -1 (DP), 0 (VHS), and 2 (FB). Here, the curves with wine spheres and green stars indicate the ascending and descending branches, respectively. As in Fig. 2, we also find the first-order transition in Fig. 3, i.e., the discontinuities in the plots of Δ_{imp} , E_{YSR} and $\mathcal{F} - \mathcal{F}_0$ versus J . For the DP $\mu = -1$, the decreasing of Δ_{imp} when raising J is much more rapid than in the cases of other μ values. The Δ_{imp} values at $\mu = -2, 0$ and 2 are more enhanced than in Fig. 2(a-c) with $g = 2$.

Interestingly, we find that J_{c1} , J_{c2} , and the estimated conventional J_c vary with g . In Fig. 3 with $g = 3$, their values for $\mu = -2, 0$ and 2 are $J_{c1} = 2.34, 2.24$ and 1.63 while $J_{c2} = 1.98, 1.73$ and 0.81 , respectively. The corresponding estimated conventional J_c for these μ are

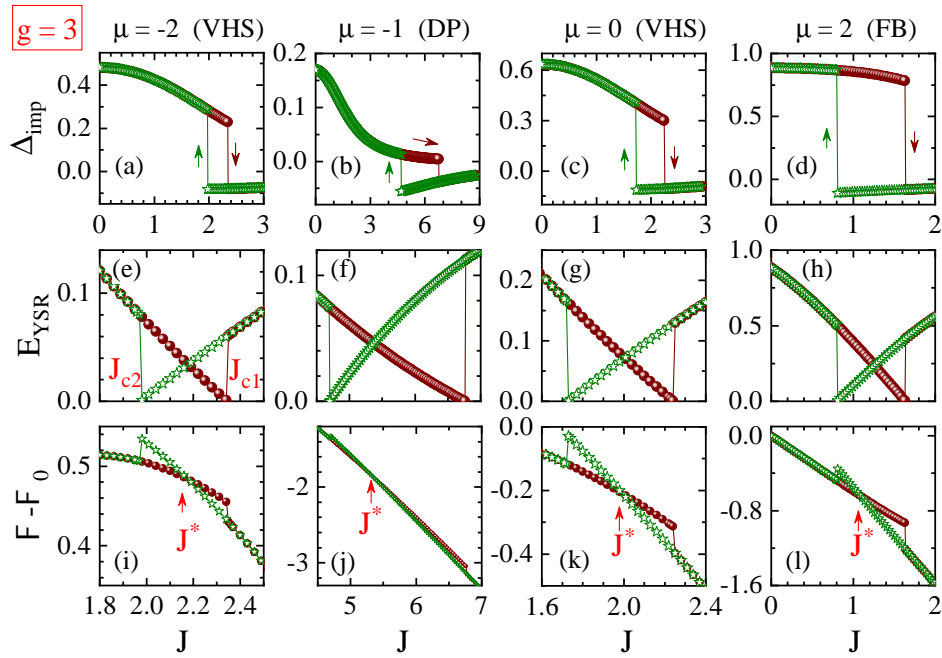


FIG. 3. (Color online) The same as in Fig. 2, but for $g = 3$. Panels (b, f, j) are the results for $\mu = -1$ (DP). The ascending and descending branches are shown as curves with wine spheres and green stars, respectively.

2.21, 2.00 and 1.06, which are located between J_{c1} and J_{c2} . But, for $\mu = -1$ (DP) the estimated conventional J_c is greater than J_{c1} while here $J_{c1} = 6.76$, $J_{c2} = 4.70$ and the estimated $J_c = 12.48$. At last, for all these four μ values, the free energies of both the ascending and descending branches cross each other at J^* , although these branches are very close for $\mu = 1$. Therefore, all these minimal stable E_{YSR} values can not reach zero, which agrees with the case of $g = 2$ in Fig. 2.

Now, we illustrate the details of the μ -dependent upper and lower critical interactions J_{c1} (curves with black squares), J_{c2} (curves with blue spheres), and the crossover interaction J^* (curves with red stars) for $g = 2$ and 3 at $T = 0$ in Figs. 4(a, b). And, the minimal stable $E_{\text{YSR},\text{min}}$ at J^* for $g = 2$ and 3 are shown in Figs. 4(c, d). The other calculation parameters are the same as in Figs. 1–3. For $g = 2$ in Fig. 4(a) and (c), the blue and green regions in these plots are the regimes with zero Δ and the electron full-filling level according to Fig. 1, respectively.

Generally, the global profiles of J_{c1} , J_{c2} and J^* in Fig. 4(a) are similar to the results of J_c in Fig. 2(b) of Ref. [27]. However, there are three major differences for $g = 2$ in our results: the first point is the absence of the J^* in the zero- Δ blue region around $\mu = -1$, the second is the exceeding of μ_{max} over $\mu = 2$, and the last point is the physics among J_{c1} , J_{c2} , J^* and J_c . Remind that J_{c1} and J_{c2} correspond to the zero- E_{YSR} solutions in the ascending and descending branches of the first-order-transition procedure, as seen in Figs. 1 and 2. In Fig. 4(a), the difference between J_{c1} and J_{c2} increases with μ , and it reaches the maximum around the FB (i.e.,

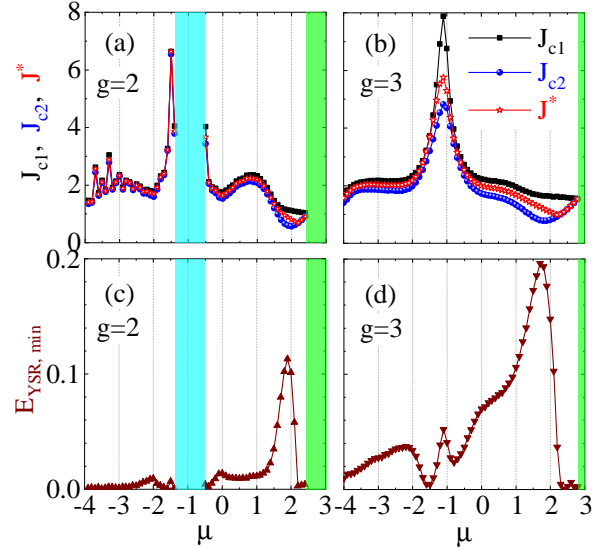


FIG. 4. (Color online) The upper and lower critical interactions J_{c1} , J_{c2} and crossover interaction J^* (a, b), the minimal stable $E_{\text{YSR},\text{min}}$ (c, d) as functions of μ for $g = 2$ and 3 at $T = 0$. The green regions on the left side of all the panels are the electron full-filling regime, while the blue regions with $g = 2$ in panels (a, c) are non-superconducting, i.e., with zero Δ , according to Fig. 1(b).

$\mu = 2$). And, in literature [21, 27], E_{YSR} is equal to zero at J_c while here J^* is the crossover interaction at which the minimal stable $E_{\text{YSR},\text{min}}$ happens. We can see in Fig. 4(a) that J^* is situated between J_{c2} and J_{c1} . More-

over, $E_{\text{YSR},\text{min}}$ in Fig. 4(c) for $g = 2$ is non-zero around $\mu = -2$ and $-0.5 < \mu < 2.2$. In particular, its local maxima are located around the two VHS points and the FB, i.e., $\mu = -2, 0$ and 2 . And, the maximal value of $E_{\text{YSR},\text{min}}$ goes up to 0.11 at $\mu = 1.9$. In Fig. 4(b), we find the complete profiles of J_{c1} , J_{c2} and J^* at μ from -4 to $\mu_{\text{max}} = 2.75$ because the superconductivity is achieved for $g = 3$ shown in Fig. 1(b). And, the significant difference between J_{c1} and J_{c2} occurs around the DP ($\mu = -1$) and FB ($\mu = 2$). As seen in Fig. 4(d), $E_{\text{YSR},\text{min}}$ for $g = 3$ is equal to zero only in the vicinity of $\mu = -1.5$ and 2.5 , while its maximum is 0.20 at $\mu = 1.7$ and two local minima at $\mu = -2.2$ and -1.1 .

IV. CONCLUSIONS

In conclusion, based on the self-consistent Bogoliubov-de Gennes equations, we have numerically studied the superconducting properties of the Yu-Shiba-Rusinov (YSR) states in the s -wave superconducting kagome Hubbard model. Similar to the density of states, the bulk superconducting pair potential changes with the chemical potential μ and reaches local maxima when μ is located at

the van Hove singularities (VHS) and the flat band (FB).

When varying the spin-magnetic interaction J of the magnetic impurity, a first-order phase transition occurs since hysteresis loops with discontinuities in the local pair potential at the impurity and the YSR-state energy E_{YSR} at the upper and lower critical potentials (J_{c1} and J_{c2}), which correspond to $E_{\text{YSR}} = 0$. The conventional critical interaction J_c is normally situated between J_{c1} and J_{c2} , except at the DP. And, the minimal stable $E_{\text{YSR},\text{min}}$ values at the crossover interaction (J^*) along the free-energy favorite path are non-zero for μ at the VHS, DP, and FB. Moreover, J_{c1} , J_{c2} and J^* depend on μ and the superconducting coupling g . Our findings can be helpful for future experiments on the YSR states in the s -wave superconducting kagome system achieved by superconducting proximity effects.

ACKNOWLEDGMENTS

This work was supported by the Science Foundation of Zhejiang Sci-Tech University (ZSTU) (Grants No. 19062463-Y) and funded within the framework of the HSE University Basic Research Program.

-
- [1] H.-M. Guo and M. Franz, Topological insulator on the kagome lattice, *Phys. Rev. B* **80**, 113102 (2009).
 - [2] W.-H. Ko, P. A. Lee, and X.-G. Wen, Doped kagome system as exotic superconductor, *Phys. Rev. B* **79**, 214502 (2009).
 - [3] M. L. Kiesel, R. Thomale, Sublattice interference in the kagome Hubbard model, *Phys. Rev. B* **86**, 121105 (2012).
 - [4] W.-S. Wang, Z.-Z. Li, Y.-Y. Xiang, and Q.-H. Wang, Competing electronic orders on kagome lattices at van Hove filling, *Phys. Rev. B* **87**, 115135 (2013).
 - [5] L. Ye, M. Kang, J. Liu, F. von Cube, C. R. Wicker, T. Suzuki, C. Jozwiak, A. Bostwick, E. Rotenberg, D. C. Bell, L. Fu, R. Comin, and J. G. Checkelsky, Massive Dirac fermions in a ferromagnetic kagome metal, *Nature* **555**, 638 (2018).
 - [6] B. R. Ortiz, L. C. Gomes, J. R. Morey, M. Winiarski, M. Bordelon, J. S. Mangum, I. W. H. Oswald, J. A. Rodriguez-Rivera, J. R. Neilson, S. D. Wilson, E. Ertekin, T. M. McQueen, and E. S. Toberer, New kagome prototype materials: Discovery of KV_3Sb_5 , RbV_3Sb_5 , and CsV_3Sb_5 , *Phys. Rev. Materials* **3**, 094407 (2019).
 - [7] B. R. Ortiz, S. M. L. Teicher, Y. Hu, J. L. Zuo, P. M. Sarte, E. C. Schueller, A. M. M. Abeykoon, M. J. Krogstad, S. Rosenkranz, R. Osborn, R. Seshadri, L. Balents, J. He, and S. D. Wilson, CsV_3Sb_5 : A Z_2 Topological Kagome Metal with a Superconducting Ground State, *Phys. Rev. Lett.* **125**, 247002 (2020).
 - [8] Y. Hu, X. Wu, B. R. Ortiz, S. Ju, X. Han, J. Ma, N. C. Plumb, M. Radovic, R. Thomale, S. D. Wilson, A. P. Schnyder, and M. Shi, Rich nature of Van Hove singularities in Kagome superconductor CsV_3Sb_5 , *Nat. Commun.* **13**, 2220 (2022).
 - [9] P. Wang, Y. Wang, B. Zhang, Y. Li, S. Wang, Y. Wu, H. Zhu, Y. Liu, G. Zhang, D. Liu, Y. Xiong, and Z. Sun, Experimental Observation of Electronic Structures of Kagome Metal YCr_6Ge_6 , *Chinese Phys. Lett.* **37**, 087102 (2020).
 - [10] G. Pokharel, S. M. L. Teicher, B. R. Ortiz, P. M. Sarte, G. Wu, S. Peng, J. He, R. Seshadri, and S. D. Wilson, Electronic properties of the topological kagome metals YV_6Sn_6 and GdV_6Sn_6 , *Phys. Rev. B* **104**, 235139 (2021).
 - [11] K. Y. Chen, N. N. Wang, Q. W. Yin, Y. H. Gu, K. Jiang, Z. J. Tu, C. S. Gong, Y. Uwatoko, J. P. Sun, H. C. Lei, J. P. Hu, and J.-G. Cheng, Double Superconducting Dome and Triple Enhancement of T_c in the Kagome Superconductor CsV_3Sb_5 under High Pressure, *Phys. Rev. Lett.* **126**, 247001 (2021).
 - [12] C. Mielke, D. Das, J.-X. Yin, H. Liu, R. Gupta, Y.-X. Jiang, M. Medarde, X. Wu, H. C. Lei, J. Chang, P. Dai, Q. Si, H. Miao, R. Thomale, T. Neupert, Y. Shi, R. Khasanov, M. Z. Hasan, H. Luetkens, and Z. Guguchia, Time-reversal symmetry-breaking charge order in a kagome superconductor, *Nature* **602**, 245 (2022).
 - [13] L. Nie, K. Sun, W. Ma, D. Song, L. Zheng, Z. Liang, P. Wu, F. Yu, J. Li, M. Shan, D. Zhao, S. Li, B. Kang, Z. Wu, Y. Zhou, K. Liu, Z. Xiang, J. Ying, Z. Wang, T. Wu, and X. Chen, Charge-density-wave-driven electronic nematicity in a kagome superconductor, *Nature* **604**, 59 (2022).
 - [14] H. Chen, H. Yang, B. Hu, Z. Zhao, J. Yuan, Y. Xing, G. Qian, Z. Huang, G. Li, Y. Ye, S. Ma, S. Ni, H. Zhang, Q. Yin, C. Gong, Z. Tu, H. Lei, H. Tan, S. Zhou, C. Shen, X. Dong, B. Yan, Z. Wang, and H.-J. Gao, Roton pair density wave in a strong-coupling kagome superconductor, *Nature* **599**, 222 (2021).
 - [15] F. H. Yu, D. H. Ma, W. Z. Zhuo, S. Q. Liu, X. K. Wen,

- B. Lei, J. J. Ying, and X. H. Chen, Unusual competition of superconductivity and charge-density-wave state in a compressed topological kagome metal, *Nat Commun* **12**, 3645 (2021).
- [16] H.-S. Xu, Y.-J. Yan, R. Yin, W. Xia, S. Fang, Z. Chen, Y. Li, W. Yang, Y. Guo, and D.-L. Feng, Multiband Superconductivity with Sign-Preserving Order Parameter in Kagome Superconductor CsV_3Sb_5 , *Phys. Rev. Lett.* **127**, 187004 (2021).
- [17] R. Gupta, D. Das, C. H. Mielke III, Z. Guguchia, T. Shiroka, C. Baines, M. Bartkowiak, H. Luetkens, R. Khasanov, Q. Yin, Z. Tu, C. Gong, and H. Lei, Microscopic evidence for anisotropic multigap superconductivity in the CsV_3Sb_5 kagome superconductor, *npj Quantum Mater.* **7**, 49 (2022).
- [18] L. Yu, Bound State in Superconductors With Paramagnetic Impurities, *Acta Phys. Sin.* **21**, 75 (1965).
- [19] H. Shiba, Classical Spins in Superconductors, *Prog. Theor. Phys.* **40**, 435 (1968).
- [20] A. I. Rusinov, Theory of gapless superconductivity in alloys containing paramagnetic impurities, *Sov. Phys. JETP* **29**, 1101 (1969).
- [21] A. V. Balatsky, I. Vekhter, and J.-X. Zhu, Impurity-induced states in conventional and unconventional superconductors, *Rev. Mod. Phys.* **78**, 373 (2006).
- [22] A. Y. Kitaev, Unpaired Majorana fermions in quantum wires, *Phys.-Usp.* **44**, 131 (2001).
- [23] D. K. Morr, N. A. Stavropoulos, Quantum interference between impurities: Creating novel many-body states in s -wave superconductors, *Phys. Rev. B* **67**, 020502 (2003).
- [24] T.-P. Choy, J. M. Edge, A. R. Akhmerov, and C. W. J. Beenakker, Majorana fermions emerging from magnetic nanoparticles on a superconductor without spin-orbit coupling, *Phys. Rev. B* **84**, 195442 (2011).
- [25] S. Nadj-Perge, I. K. Drozdov, B. A. Bernevig, and A. Yazdani, Proposal for realizing Majorana fermions in chains of magnetic atoms on a superconductor, *Phys. Rev. B* **88**, 020407 (2013).
- [26] J. Klinovaja, P. Stano, A. Yazdani, and D. Loss, Topological Superconductivity and Majorana Fermions in RKKY Systems, *Phys. Rev. Lett.* **111**, 186805 (2013).
- [27] S. Basak, A. Ptok, Shiba states in systems with density of states singularities, *Phys. Rev. B* **105**, 094204 (2022).
- [28] S. Głodzik and A. Ptok, Quantum phase transition induced by magnetic impurity, *J. Supercond. Nov. Magn.* **31**, 647 (2018).
- [29] M. I. Salkola, A. V. Balatsky, and J. R. Schrieffer, Spectral properties of quasiparticle excitations induced by magnetic moments in superconductors, *Phys. Rev. B* **55**, 12648 (1997).
- [30] Y.-H. Lin, C.-J. Chen, N. Kumar, T.-Y. Yeh, T.-H. Lin, S. Blügel, G. Bihlmayer, and P.-J. Hsu, Fabrication and Imaging Monatomic Ni Kagome Lattice on Superconducting $\text{Pb}(111)$, *Nano Lett.* **22**, 8475 (2022).
- [31] L. Farinacci, G. Reecht, F. von Oppen, and K. J. Franke, Yu-Shiba-Rusinov bands in a self-assembled kagome lattice of magnetic molecules, [arxiv:2307.09993](https://arxiv.org/abs/2307.09993) (2023).
- [32] F. H. L. Essler, H. Frahm, F. Gohmann, A. Klumper, and V. E. Korepin, *The One-dimensional Hubbard Model* (Cambridge University Press, 2005).
- [33] We have verified that the sign before $(K - \sigma J)\delta_{i0}$ should be a minus, which is different from Eq. (7) in Ref. [27].
- [34] P. G. De Gennes, Boundary Effects in Superconductors, *Rev. Mod. Phys.* **36**, 225 (1964).
- [35] J. B. Ketterson, S. N. Song, *Superconductivity* (Cambridge, 1999).
- [36] I. Kosztin, Š. Kos, M. Stone, and A. J. Leggett, Free energy of an inhomogeneous superconductor: A wavefunction approach, *Phys. Rev. B* **58**, 9365 (1998).
- [37] Y. Chen, M. D. Croitoru, A. A. Shanenko, and F. M. Peeters, Superconducting nanowires: Quantum confinement and spatially dependent Hartree-Fock potential, *J. Phys. Condens. Matter* **21**, 435701 (2009).
- [38] Y. Chen, A. A. Shanenko, M. D. Croitoru, and F. M. Peeters, Quantum cascades in nano-engineered superconductors: Geometrical, thermal and paramagnetic effects, *J. Phys. Condens. Matter* **24**, 265702 (2012).
- [39] Y. Chen, A. A. Shanenko, and F. M. Peeters, Vortex anomaly in low-dimensional fermionic condensates: Quantum confinement breaks chirality, *Phys. Rev. B* **89**, 054513 (2014).
- [40] L. Yin, Y. Bai, M. Zhang, A. A. Shanenko, and Y. Chen, Surface superconductor-insulator transition induced by electric field, *Phys. Rev. B* **108**, 054508 (2023).
- [41] Y. Chen, Q. Zhu, M. Zhang, X. Luo, and A. A. Shanenko, Surface superconductor-insulator transition: Reduction of the critical electric field by Hartree-Fock potential, *Physics Letters A* **494**, 129281 (2024).
- [42] Y. Bai, Y. Chen, M. D. Croitoru, A. A. Shanenko, X. Luo, and Y. Zhang, Interference-induced surface superconductivity: Enhancement by tuning the Debye energy, *Phys. Rev. B* **107**, 024510 (2023).
- [43] Y. Bai, L. Zhang, X. Luo, A. A. Shanenko, and Y. Chen, Tailoring of interference-induced surface superconductivity by an applied electric field, *Phys. Rev. B* **108**, 134506 (2023).